Surface-emitting second-harmonic generation in AlGaAs/GaAs waveguides

C. DEGEN[1]*, G. JENNEMANN[1], I. FISCHER[1], W. ELSÄßER[1], S. LEU[2], R. RETTIG[2] AND W. STOLZ[2]

[1]*Institut für Angewandte Physik, Technische Universität Darmstadt, Schloßgartenstr. 7, 64289 Darmstadt, Germany;*
[2]*Wissenschaftliches Zentrum für Materialwissenschaften, Philipps-Universität Marburg, Hans-Meerwein-Straße, 35032 Marburg, Germany*
(*author for correspondence: E-mail: elsaesser@physik.tu-darmstadt.de)

Abstract. We investigate the impact of waveguide properties on the performance of surface-emitting second-harmonic generation (SESHG) devices. Using multi-layer AlGaAs/GaAs ridge waveguides that are optimized for SESHG at fundamental wavelengths $\lambda_\omega = 1060$ and 1550 nm, we achieve nonlinear cross-sections among the highest reported so far. In these devices, characteristics of the guided fundamental wave strongly determine the SESHG performance: multiple reflections in the longitudinal direction affect the conversion efficiency while higher order lateral waveguide modes modify the SESHG farfield. Both effects are significant for applications of SESHG in integrated photonic circuits.

Key words: nonlinear optics, second-harmonic generation, semiconductor waveguides, SESHG

1. Introduction

Generation of harmonic waves is one of the key processes in nonlinear optics. Only a few years after the first demonstration of optical second-harmonic generation (SHG) in bulk nonlinear media (Franken *et al.* 1961), SHG at interfaces was found (Bloembergen *et al.* 1969). However, it took 10 more years to improve the extremely low conversion efficiencies by introducing the concept of surface-emitting second-harmonic generation (SESHG) based on counter-propagating fundamental waves in optical waveguides. The first set-ups used Ti:LiNbO$_3$ waveguides to demonstrate optical pulse processing (Normandin *et al.* 1979, 1980; Stegeman *et al.* 1981, 1982). The transfer of SESHG to the GaAs/AlGaAs material system significantly promoted the perspectives for integration with other photonic devices (Vakhshoori *et al.* 1988). The demonstrated applications include a surface-emitting sum-frequency generation-based spectrometer (Vakhshoori *et al.* 1989a) and a SES-HG-based optical correlator (Vakhshoori *et al.* 1989b). Considerable enhancement of SESHG efficiency was obtained by using quasi-phase-matched multi-layer waveguides (Normandin *et al.* 1991; Whitbread *et al.* 1994). In

this geometry, multiple interfaces are incorporated in a single waveguide, such that their respective SESHG signals add up coherently to a total harmonic wave. Further developments included crystal orientations deviating from the commonly used (1 0 0)-GaAs substrates (Vakhshoori *et al.* 1991; Whitbread *et al.* 1993), intra-cavity integration of the multi-layer stack in an edge-emitting diode laser (Dai *et al.* 1992; Ramos *et al.* 1996), and integration of a vertical cavity for the harmonic waves (Lodenkamper *et al.* 1993; Ding *et al.* 1995; Janz *et al.* 1997). For the passive devices, it was still necessary to use short-pulse laser systems to provide high peak powers at the fundamental wavelength.

We have followed the approach of Whitbread *et al.* (1994) to optimize the design of an GaAs/AlGaAs-based waveguide for SESHG at the important wavelengths $\lambda_\omega = 1060$ and 1550 nm. By careful design modifications we have improved the frequency conversion performance such, that for the first time we can use semiconductor lasers under cw-operation to generate harmonic signals of up to 1 nW. This amount of power is sufficiently high for quantitative measurements and a detailed analysis of the spatial emission properties. In particular, we investigate the consequences of longitudinal effects such as multiple internal reflections of the fundamental wave, and lateral effects like higher order waveguide modes on SESHG performance. Thus, our work is a significant step towards the utilization of waveguide-based SESHG in integrated photonic circuits.

The paper is organized as follows. In Section 2, we revise our modelling which results in the final device design and we discuss further optimization steps. In Section 3, we introduce the experimental setup (3.1) and characterize the nonlinear waveguide by measurements of the nonlinear cross-section (3.2). Moreover, the influence of birefringence on the SESHG nearfield (3.3) and of transverse waveguide modes on the farfield (3.4) are discussed.

2. Waveguide optimization

The optimization of a multi-layer waveguide for SESHG requires the consideration of numerous antagonistic aspects. For practical reasons we use AlGaAs on (1 0 0)-GaAs substrate as material system. Moreover, to keep the structure tolerant against wavelength changes of the fundamental signal, we have decided not to integrate a vertical cavity for the harmonic wave (Lodenkamper *et al.* 1993; Ding *et al.* 1995; Janz *et al.* 1997). Thus, the basic layout of the guiding region consists of several alternating AlGaAs layers with different aluminum content. We have chosen $Al_{0.8}Ga_{0.2}As$/GaAs in order to obtain a large difference in the nonlinear susceptibilities of the involved materials. However, for both fundamental wavelengths considered, $\lambda_\omega = 1060$ and 1550 nm, the energies of the respective second-harmonic waves are larger than the band-gap energy of GaAs so that they experience

absorption. Thus, increasing the number of layers increases internal absorption losses. On the other hand, the strength of the generated harmonic signal increases with the number of layers because the number of radiating interfaces increases. We adopt the algorithm of Whitbread *et al.* (1994) to determine the optimum number and thicknesses of the respective layers for a maximum conversion efficiency of the waveguide. The algorithm is based on scattering matrices and serves to calculate the propagating fields inside the structure, including the boundary conditions for TE and TM polarized light. Then, a Greens-function approach is used to calculate the desired design parameters, taking into account multiple reflections of the generated second-harmonic light at all involved vertical material interfaces of the waveguide as well as absorption of the harmonic light in the semiconductor crystal. Material parameters used for the modelling are taken from Adachi (1985).

We have carried out the optimization algorithm for both fundamental wavelengths under consideration. The optimum layout for both cases consists of three layers of GaAs separated by two layers of $Al_{0.8}Ga_{0.2}As$. The thicknesses d of the layers correspond to half the harmonic wavelengths in the respective materials, i.e., $d_{GaAs}(1060 \text{ nm}) = 64 \text{ nm}$, $d_{GaAs}(1550 \text{ nm}) = 106 \text{ nm}$, $d_{Al_{0.8}Ga_{0.2}As}(1060 \text{ nm}) = 76 \text{ nm}$, $d_{Al_{0.8}Ga_{0.2}As}(1550 \text{ nm}) = 121 \text{ nm}$. This multilayer stack is the core of the planar waveguide. Beneath, we have placed a $(5\lambda_{2\omega})$-thick spacing layer to avoid losses due to substrate modes. Next, a stack of twelve $(\lambda_{2\omega}/4)$ GaAs/AlAs layers is placed below the spacer. This stack acts as Bragg-reflector for the substrate-directed fraction of the second-harmonic light. On top of the waveguide core, we have added a $(4\frac{1}{4}\lambda_{2\omega})$ $Al_{0.8}Ga_{0.2}As$ layer as anti-reflection coating to achieve a better outcoupling of the second-harmonic light into air. A 5 nm-thick GaAs-layer serves as protection cap.

These so optimized multi-layer waveguides have been grown using MOCVD. After growth, the wafers have been photo-lithographically processed to define waveguide ridges which then have been etched wet-chemically into the planar waveguides. The ridges are 10 μm wide and 500 nm high and provide efficient lateral confinement to the fundamental field. As a last step, we have cleaved the wafer to define the facets through which the fundamental power will be coupled in. The lengths of the resulting ridge waveguides vary from below one millimeter to several millimeters. Fig. 1 depicts a scanning electron microscope picture of the cleaved waveguide facet.

3. Experiment

3.1. EXPERIMENTAL SETUP

The scheme of our experimental setup is shown in Fig. 2. We use a symmetric configuration of two lasers in order to maximize the total amount of
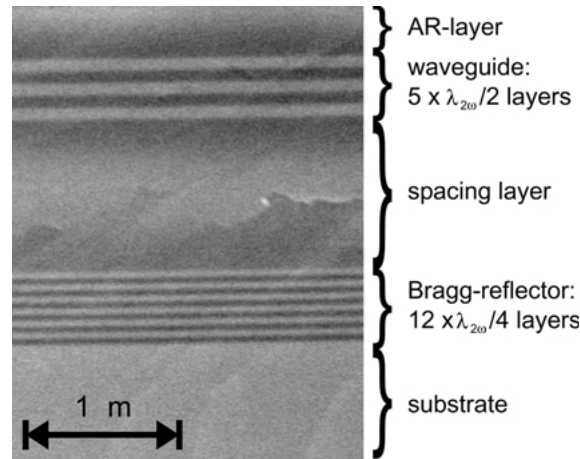
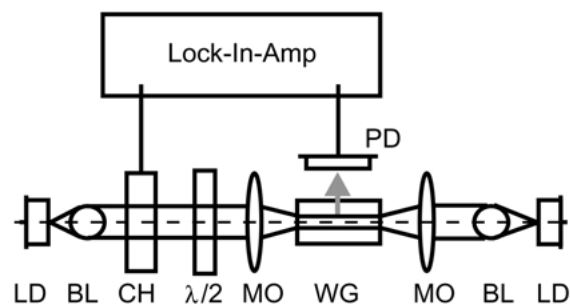Fig. 1. Cross-section of a multi-layer waveguide (scanning electron microscopy image).

Fig. 2. Experimental setup. LD: laser diode, BL: ball-lens, CH: chopper, $\lambda/2$: half-wave plate, MO: microscope objective, WG: waveguide, PD: photodetector.

counter-propagating fundamental power in the waveguide. Two pairs of identical diode lasers (LD) at center-wavelengths of $\lambda_\omega = 1058$ nm (multi-mode) or $\lambda_\omega = 1555$ nm (singlemode) generate the fundamental field with maximum powers P_{ld} of 100 and 30 mW, respectively. The light from the diode lasers is collimated by antireflection coated ball-lenses. We use a half-wave plate ($\lambda/2$) to rotate the polarization state of one laser beam from TE to TM polarization as required for SESHG in (1 0 0)-oriented crystals. The fundamental light is coupled into the waveguide ridge (WG) using microscope objectives (MO). The generated harmonic light is detected with a calibrated photodetector (APD). We assure the correct calibration by cross-checking a large area avalanche photodiode (Advanced Photonix) and a Si-PIN diode (EG&G HUV-4000). The use of lock-in technique and a chopper (CH) improves the signal to noise ratio of the measurements. For the analysis of the near-field's spatial structure, we project the surface of the

waveguide onto a CCD-camera or onto a photographic film. The farfield is recorded directly in the propagating field without projection lenses.

3.2. NONLINEAR CROSS-SECTION A^{nl}

In Fig. 3, we plot the power of the detected second-harmonic, P^{SH}, versus the square of the pump laser optical power, P_{ld}^2. The left part depicts results for $\lambda_\omega = 1060$ nm and a ridge length $L = 3.07$ mm (a), while the right part contains results for $\lambda_\omega = 1550$ nm, $L = 0.93$ mm (b) and $L = 2.88$ mm (c). The solid curves have been obtained from the measured values by spline-interpolation while the dashed lines are linear fits to the maxima of the solid curves. The results for $\lambda_\omega = 1060$ nm (a) are in good agreement with the linear fit curve, as expected for a second-order nonlinear effect. For the curves (b) and (c) in contrast, a distinct periodic deviation from the linear dependence is visible. This periodic deviation is caused by the interaction of two effects. Firstly, the parallel waveguide facets with a power reflectivity of $R = 0.3$ act as mirrors of a planar Fabry-Perot interferometer. Secondly, the diode lasers' emission wavelengths shift continuously with increasing injection current because they are operated at constant temperature. Due to this spectral variation, several Fabry-Perot resonances are scanned through in the operation range under consideration. Thus, the fundamental power shows resonant enhancements which again modulate the second-harmonic power. The resonance spacing of a planar Fabry-Perot interferometer with $L = 0.93$ mm amounts to 0.37 nm. The wavelength shift of the used diode laser amounts to 0.92 nm which is equivalent to 2.5 Fabry-Perot periods (2.5 periods in Fig. 3(b)). For $L = 2.88$ mm, one expects 7.7 periods which again
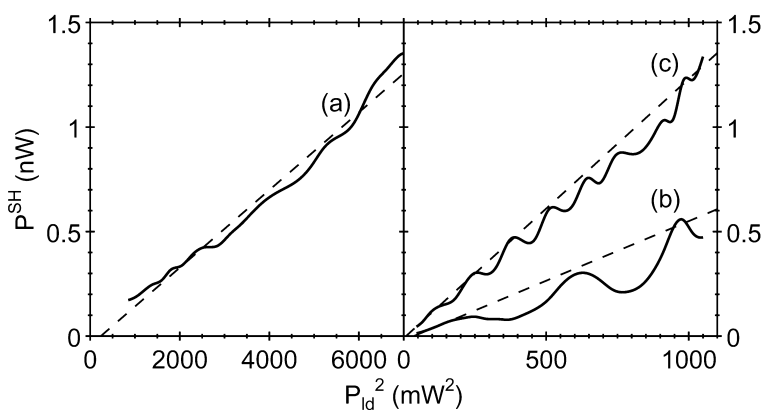

Fig. 3. Detected harmonic power versus squared laser diode optical power. The solid lines are spline-interpolations of the experimental values, the dashed lines are linear fit curves to the resonance maxima. The labels indicate (a): $\lambda_\omega = 1060$nm and ridge-length $L = 3.07$ mm, (b): $\lambda_\omega = 1550$ nm and $L = 0.93$ mm, (c): $\lambda_\omega = 1550$ nm and $L = 2.88$ mm.

agrees with our observations (Fig. 3(c)). For $\lambda_\omega = 1060$ nm (Fig. 3(a)), no periodic variation is visible because the diode lasers at this wavelength emit multiple modes and consequently, the Fabry-Perot effect is washed out.

The pronounced Fabry-Perot effect of the ridge waveguide shows clearly the need to account for multiple internal reflections at the waveguide facets when calculating the peak nonlinear cross-section A^{nl}, defined by (Beaulieu *et al.* 1995)

$$P^{\mathrm{SH}} = A^{\mathrm{nl}} P^+ P^- \frac{L}{w}, \tag{1}$$

where P^{SH} is the resonance enhanced second-harmonic power, P^+ and P^- are the powers of the counter-propagating guided waves in the ridge, L is the length of the waveguide in centimeters, and w is the width of the waveguide in millimeters. Considering multiple reflections and relating P^{SH} to the laser output power P_{ld}, Equation (1) becomes

$$P^{\mathrm{SH}} = A^{\mathrm{nl}} \left(2.1 \eta^2 P_{\mathrm{ld}}^2 \right) \frac{L}{w}. \tag{2}$$

Here, η is the coupling efficiency into the waveguide, depending on the diode lasers' beam profile. The factor 2.1 arises from the infinite series of the internal reflections with a power reflectivity $R = 0.3$: $\left(\sum_{n=0}^{\infty} R^n \right)^2 = 1/(1-R)^2 = 2.1$. To determine A^{nl} of the respective waveguide structures, we use the slope $P^{\mathrm{SH}}/P_{\mathrm{ld}}^2$ of the linear fit curves in Fig. 3 in the re-ordered Equation (2)

$$A^{\mathrm{nl}} = \left(\frac{1}{2.1\eta^2} \frac{w}{L} \right) \frac{P^{\mathrm{SH}}}{P_{\mathrm{ld}}^2}. \tag{3}$$

Considering $\eta = 0.01 \ldots 0.025$, depending on the lasers' beam profile, and normalizing to the respective ridge dimensions, we obtain nonlinear cross-sections $A^{\mathrm{nl}} = (3.0 \pm 0.3) \times 10^{-5}$ W^{-1} cm^{-1} mm for $\lambda_\omega = 1060$ nm and $A^{\mathrm{nl}} = (3.5 \pm 1.2) \times 10^{-5}$ W^{-1} cm^{-1} mm for $\lambda_\omega = 1550$ nm as mean values for all investigated samples at the respective wavelengths. Considering uncertainties for the calibration of the APD and for estimating the coupling efficiency, we end up with a relative uncertainty in A^{nl} of 40%. The A^{nl} in our waveguides is close to the highest reported nonlinear cross-sections $(3.9 \times 10^{-5}$ W^{-1} cm^{-1} mm at $\lambda_\omega = 1300$ nm (Frlan *et al.* 1994), 5×10^{-5} W^{-1} cm^{-1} mm at $\lambda_\omega = 1550$ nm (Janz *et al.* 1997) which are *not* corrected for multiple reflections of the fundamental wave. Considering facet reflections $(2 \times 10^{-6}$ W^{-1} cm^{-1} mm (Janz *et al.* 1997)) our results are even the highest values of A^{nl} obtained so far.

Periodic variations of the harmonic power due to multiple internal reflections of the fundamental wave might be disadvantageous for SESHG applications. The effect can be avoided by using waveguides with antireflection coated facets or by spectrally stabilizing the lasers used as sources for the fundamental power.

3.3. NEARFIELD

Since the waveguide structure is grown on (1 0 0) substrates, SESHG requires excitation of both, transverse electric (TE) and transverse magnetic (TM) modes of the waveguide (Vakhshoori *et al.* 1988). Consequently, the generated harmonic intensity varies spatially along the waveguide as

$$P^{SH} \sim \cos^2(\Delta\beta z), \tag{4}$$

where $\Delta\beta = \beta_{TE} - \beta_{TM}$ denotes the difference in the propagation constants for TE and TM mode, a measure for the crystals birefringence, and the coordinate z denotes the position along the waveguide.

Fig. 4 depicts nearfield patterns of the SESHG for the fundamental wavelengths $\lambda_\omega = 1060$ nm (top) and $\lambda_\omega = 1550$ nm (bottom). The guided wave is propagating from the left to the right and vice versa. The modulation of period $\cos^2(\Delta\beta z)$ is clearly visible. Thus, it is possible to determine from the geometrical period Λ of the modulation the difference of the propagation constants, $\Delta\beta$, using

$$\Delta\beta = \pi/\Lambda. \tag{5}$$

The width of the waveguide ridge is known from scanning electron microscope pictures to amount to 10 μm whereas the ridges are separated by 20 μm wide grooves. With these values as scale we obtain from Fig. 4, $\Lambda = 20$ μm ($\lambda_\omega = 1060$ nm) and $\Lambda = 30$ μm ($\lambda_\omega = 1550$ nm), resulting in $\Delta\beta = 157$ rad/mm ($\lambda_\omega = 1060$ nm) and $\Delta\beta = 105$ rad/mm ($\lambda_\omega = 1550$ nm). To our
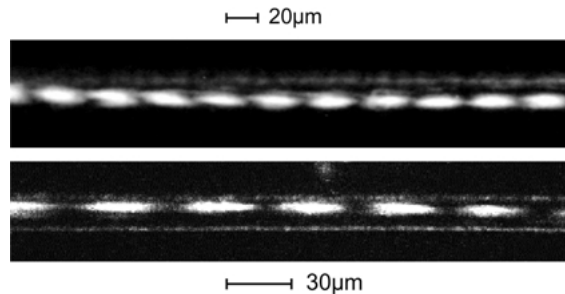

Fig. 4. Nearfield images of SESHG at $\lambda_\omega = 1060$ nm (top) and $\lambda_\omega = 1550$ nm (bottom).

knowledge, these are the first experimentally obtained values for the given material system at the important wavelength of $\lambda = 1550$ nm. Calculations for $\lambda_\omega = 1060$ nm in a corresponding structure result in a geometrical period of $\Lambda_{1060\,\mathrm{nm}} = 18.4\,\mu\mathrm{m}$ (Whitbread *et al.* 1994), which agrees well with our experimental value of $\Lambda = 20\,\mu\mathrm{m}$.

The magnitude of birefringence in the waveguide is relevant for example in SESHG-based optical correlators (Vakhshoori *et al.* 1989b). In the $(1\,0\,0)$-crystal, birefringence may lead to a broadening of the fundamental light pulses, thus affecting the correlator's temporal resolution and thus has to be considered in calculating the pulse widths. Moreover, the geometrical period of the nearfield intensity modulation also determines the farfield which will be discussed in the next paragraph.

3.4. FARFIELD

The SESHG nearfield shown in Fig. 4 exhibits a periodic spatial intensity variation determined by Equation (4). Corresponding to this intensity distribution, one expects a farfield pattern consisting of parallel lines orthogonal to the waveguide ridge. The upper part of Fig. 5 is an image of the SESHG farfield, which indeed consists of lines roughly orthogonal to the ridge. However, the lines are not exactly parallel but slightly mutually tilted. This deviation from the expected farfield is indication that the nearfield contains additional structures, presumably in the lateral direction. Indeed, careful evaluation of the nearfield images yields that locally, higher order lateral waveguide modes are excited. This is evident from the lower part of Fig. 5: the nearfield of the SESHG acts as a probe for the excited waveguide modes of the fundamental wave.

Since the mutual tilting of the farfield lines generally increases the divergence of the radiated signal, the presence of lateral waveguide modes is relevant for SESHG applications. In SESHG-based spectrometers (Vakhshoori *et al.* 1989a), the spectral resolution depends on the farfield properties. Thus, to obtain the highest possible resolution, the width of the ridge waveguide should be reduced such that only the fundamental lateral mode is guided. In this way, the farfield divergence angle in the direction along the ridge is minimized. The simultaneous reduction of coupling efficiency seems to be unavoidable for a high spectral resolution device.

4. Summary

We have presented detailed characterization measurements on multi-layer waveguides that have been optimized for SESHG. The nonlinear cross-sections are among the highest obtained so far and enable us to use diode lasers
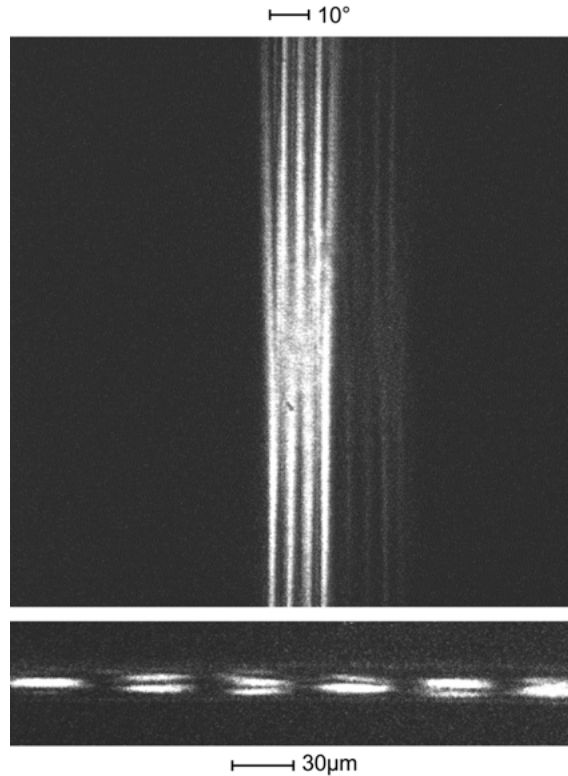
Fig. 5. Farfield (top) and nearfield (bottom) of SESHG at $\lambda_\omega = 1550$ nm in $10\,\mu$m wide waveguide ridge

under cw-operation to provide the fundamental wave. Characteristics of the ridge waveguide strongly determine the SESHG performance: multiple internal reflections of the fundamental wave at the facets affect the conversion efficiency, whereas lateral waveguide effects may limit the resolution of SESHG-based integrated photonics devices.

Acknowledgements

References

Adachi, S. *J. Appl. Phys.* **58** R1, 1985.
Beaulieu, Y., S. Janz, H. Dai, E. Frlan, C. Fernando, A. Delage, P. van der Meer, M. Dion and R. Normandin. *J. Nonlinear Opt. Phys. Mater.* **4** 893, 1985.

Bloembergen, N., H.J. Simon and C.H. Lee. *Phys. Rev* **181** 1261, 1969.

Dai, H., S. Janz, R. Normandin and F. Chatenoud. *Can. J. Phys.* **70** 921, 1992.

Ding, Y.J., J.B. Khurgin and S.-J. Lee. *J. Opt. Soc. Am. B* **12** 1586, 1995.

Franken, P.A., A.E. Hill, C.W. Peters and G. Weinreich. *Phys. Rev. Lett.* **7** 118, 1961.

Frlan, E., J.S. Wight, S. Janz, H. Dai, F. Chatenoud, M. Buchanan and R. Normandin. *Opt. Lett.* **19** 1657, 1994.

Janz, S., Y. Beaulieu, A. Fiore, P. Bravetti, V. Berger, E. Rosencher and J. Nagle. *Opt. Express* **2** 462, 1997.

Lodenkamper, R., M.L. Bortz, M.M. Fejer, K. Bacher and J.S. Jr. Harris, *Opt. Lett.* **18** 1798, 1993.

Normandin, R. and G.I. Stegeman. *Opt. Lett.* **4** 58, 1979.

Normandin, R. and G.I. Stegeman. *Appl. Phys. Lett.* **36** 253, 1980.

Normandin, R., S. Letourneau, F. Chatenoud and R.L. Williams. *IEEE J. Quantum Elec.* **27** 1520, 1991.

Ramos, P.A. and E. Towe. *Appl. Phys. Lett.* **69** 3321, 1996.

Stegeman, G.I. and R. Normandin. In: *SPIE, Proceedings on Integrated Optics and Millimeter and Microwave Integrated Circuits* (eds.) B.D. Guenther and W. Pittman, Vol 317, p. 291, SPIE, 1981.

Stegeman, G.I. and R. Normandin. *SPIE, Proceedings on Integrated Optics II* D.G. Hall (ed.) Vol 321, p. 55, SPIE, 1982.

Vakhshoori, D., M.C. Wu and S. Wang. *Appl. Phys. Lett.* **52** 422, 1988.

Vakhshoori, D., J. Walker, S. Dijaili, S. Wang and J.S. Smith. *Appl. Phys. Lett.* **55** 1164, 1989a.

Vakhshoori, D., J. Walker, S. Wang, J.S. Smith, C.E. Soccolich and M.N. Islam. *Appl. Phys. Lett* **54** 1725, 1989b.

Vakhshoori, D., R.J. Fischer, M. Hong, D.L. Sivco, G.L. Zydzik, G.N.S. Chu and A.Y. Cho. *Appl. Phys. Lett.* **59** 896, 1991.

Whitbread, N.D., J.S. Roberts, P.N. Robson and M.A. Pate, *Electron. Lett.* **29** 2106, 1993.

Whitbread, N.D. and P.N. Robson *IEEE J. Quantum Elec.* **30** 139, 1994.